Dynamics of the Bacterial Flagellar Motor: The Effects of Stator Compliance, Back Steps, Temperature, and Rotational Asymmetry

Giovanni Meacci,[†‡] Ganhui Lan,[†] and Yuhai Tu[†*]
[†]IBM T. J. Watson Research Center, Yorktown Heights, New York; and [‡]Department of Biological Sciences, Columbia University, New York, New York

ABSTRACT The rotation of a bacterial flagellar motor (BFM) is driven by multiple stators tethered to the cell wall. Here, we extend a recently proposed power-stroke model to study the BFM dynamics under different biophysical conditions. Our model explains several key experimental observations and reveals their underlying mechanisms. 1), The observed independence of the speed at low load on the number of stators is explained by a force-dependent stepping mechanism that is independent of the strength of the stator tethering spring. Conversely, without force-dependent stepping, an unrealistically weak stator spring is required. 2), Our model with back-stepping naturally explains the observed absence of a barrier to backward rotation. Using the same set of parameters, it also explains BFM behaviors in the high-speed negative-torque regime. 3), From the measured temperature dependence of the maximum speed, our model shows that stator-stepping is a thermally activated process with an energy barrier. 4), The recently observed asymmetry in the torque-speed curve between counterclockwise- and clockwise-rotating BFMs can be quantitatively explained by the asymmetry in the stator-rotor interaction potentials, i.e., a quasilinear form for the counterclockwise motor and a quadratic form for the clockwise motor.

INTRODUCTION

Like all other motile bacteria, *Escherichia coli* continuously explores its environment in pursuit of favorable conditions for survival. An *E. coli* cell's swimming motion is propelled by the rotations of several flagella, each driven by a rotary flagellar motor attached to the cell body. The cell changes its swimming direction by switching its flagellar motors between counterclockwise (CCW) and clockwise (CW) rotational directions (1–3). A single flagellar motor is composed of one rotor, a circular ring structure roughly 45 nm in diameter (4), and several stator units anchored to the rigid peptidoglycan cell wall. The rotor contains a ring of ~26 FliG proteins, and each stator has four copies of protein MotA and two copies of protein MotB, forming two proton-conducting transmembrane channels. A flow of protons, driven by the electrochemical gradients across the channels, causes conformational changes of the stator proteins that generate force on the rotor through electrostatic interaction between MotA and protein FliG (5). The work/unit charge that a proton can do in crossing the cytoplasmic membrane through the proton channel is called the proton-motive force (PMF), Δp, which is ~ -170 mV for *E. coli* under normal physiological conditions (2).

The stators are tightly coupled with the rotor with a duty ratio close to unity (6). Biochemical and structural studies (7–9) indicate that torque is generated by stator conformational changes as a consequence of ion binding and unbinding to the negatively charged D32 residue on the MotB helices. It can be presumed that the passage of (one or a few) protons switches the stator to be engaged with the next FliG monomer on the FliG ring along the direction of rotation, stretching the link between the stator and the rotor. The subsequent relaxation process rotates the rotor and the attached load toward the new equilibrium position. This can give rise to a steplike motion, observed recently (10) for a sodium-powered motor at very low sodium-motive-force. However, a general understanding of the stepping dynamics of a single flagellar motor is still lacking.

The torque-speed dependence is the key biophysical property that characterizes the motor (2,11,12). For *E. coli* at room temperature under normal physiological conditions, the maximum angular velocity is ≈ 300 Hz and the estimated maximum torque ranges from 1400 pN·nm (13,14) to 4700 pN·nm (15). The measured torque-speed curve for bacterial flagellar motor in the CCW rotational state exhibits a concave shape with a plateau of high torque at low speed and a fast, quasilinear decrease of torque at high speed. Here, we use a modeling approach to understand the general underlying microscopic mechanisms responsible for different shapes (e.g., concave versus convex) of the torque-speed curve, which may be useful in understanding the dynamics of other molecular motors, such as kinesin and myosin-V, where both convex and concave force-speed curves were observed (16–18). More specific to BFM, our model is used to explain the recently observed asymmetry between the CW and CCW torque-speed curves (19).

Several mathematical models (20–25) have been proposed to describe the BFM dynamics based on assumptions about details of the electrostatic interaction between the stators and the rotor. More recent works (26–29) use a general approach independent of the details of the microscopic interactions. The model introduced by Xing et al.

Submitted November 17, 2010, and accepted for publication February 28, 2011.

*Correspondence: yuhai@us.ibm.com

Editor: R. Dean Astumian.

0006-3495/11/04/1986/10 $2.00

doi: 10.1016/j.bpj.2011.02.045

(26) can reproduce the observed torque-speed curve characteristics. However, that model predicted that the maximum velocity depends inversely on the number of stators (see the supplementary text in Xing et al. (26)), a finding that is inconsistent with the resurrection experiment of Yuan and Berg (30), which shows that the velocity of the motor is independent of the number of stators at zero load. Recently, we introduced a model for BFM where the stepping rate is higher when the stator is generating torque in the wrong direction, that is, opposite to the rotational direction of the rotor. The maximum BFM speed is independent of the number of stators in our model (31). Another possible mechanism put forth in (27,30) is the elastic interaction between the stator and its anchoring point at the rigid cell wall (32). The basic idea is that the flexible stator location enabled by a soft spring could damp the conflicting forces generated by different stators at low load. Here, we systematically study the effects of these two mechanisms to evaluate their validity.

Another important characteristic of the BFM torque-speed curve is the absence of a barrier to backward rotations, as shown in electrorotation (33) and optical tweezer (15) experiments. Here, we extend our model to include a back-stepping probability, which becomes significant as the system is driven far away from the stator-rotor equilibrium position. This extended model reproduces the absence of a barrier to backward rotation, it also explains the experiments (34) where the motor is driven forward by external force beyond its intrinsic maximum speed. Finally, the temperature dependence of the motor dynamics is studied in our model. By assuming a thermally activated stepping rate, our model reproduced the recently measured temperature dependence of the speed at near-zero load (35), from which the energy barrier for stator stepping is determined.

RESULTS

The power-stroke model of bacterial flagellar motor

We use the general model framework from our previous work (31) with several important new ingredients. We have introduced a finite probability for stator back-stepping and a stator spring connecting the stator to its anchor point on the rigid cell wall. In the model (Fig. 1 *A*), the two springs represent the load-rotor interaction and the interaction between a stator and the peptidoglycan cell wall, and the dotted curve represents the interaction potential between the rotor and a stator. The interaction between the rotor and the stators drives the rotation of the rotor. A stator stepping event results in a shift of the interaction potential in the direction of the motor rotation by an angle δ_0 and the subsequent motor motion is governed by this new potential until the next stepping event occurs. The step size $\delta_0 = \delta/2$ is set for simplicity, where $\delta = 2\pi/26$ is the angular periodicity of the FliG ring.

The dynamics of the rotor angle θ and the load angle, θ_L, can be described by the Langevin equations as first introduced in Xing et al. (26):

$$\xi_R \frac{d\theta}{dt} = -\frac{\partial}{\partial\theta}\sum_{i=1}^{N} V\left(\theta - \theta_i^S\right) - F(\theta - \theta_L) + \sqrt{2k_B T \xi_R}\,\alpha(t), \tag{1}$$

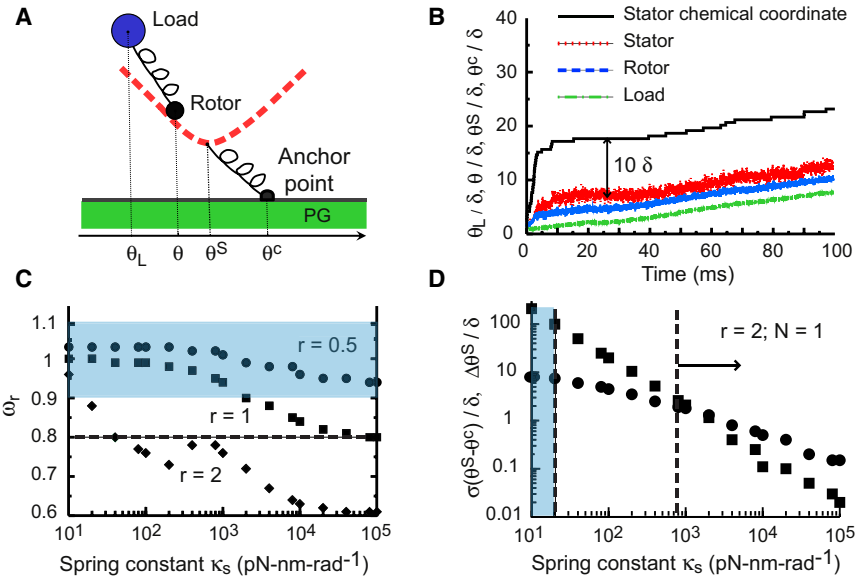

FIGURE 1 (Color online) The motor dynamics. (*A*) Illustration of the model. The load (*large circle*) is linked to the rotor (*small circle*) with a spring, and a stator is linked to the peptidoglycan cell wall (*PG*) with a spring. The dashed line represents the stator-rotor interaction potential. (*B*) The stator, rotor, and load dynamics at high load with a soft stator spring, $\kappa_S = 200$ pN·nm·rad^{-1}, for the case where $N = 1$ and $r = 2$. Starting from the top, the solid line shows the stepping dynamics of the stator's chemical coordinate, and the dotted line represents the stator's overall dynamics: internal coordinate steps plus the physical angular movements. The stretching of the stator spring at steady state is roughly 10δ. Dashed and black dash-dotted lines represent the rotor and load angular coordinates, respectively. (*C*) $\omega_r = \omega(8)/\omega(1)$ as a function of κ_S. Spheres, squares, and diamonds correspond to $r = 0.5$, $r = 1$, and $r = 2$, respectively. The dashed line represents the 20% error line with $\omega_r = 0.8$. The shaded semitransparent area represents a zero-load speed variation of 10%. (*D*) Stator displacement, $\Delta\theta^S$ (*squares*), and fluctuation, $\sigma(\theta^S - \theta^c)$ (*dots*), decrease as the stator spring constant, κ_S, increases. To keep $\Delta\theta^S$, $\sigma(\theta^S - \theta^c) \le 2\delta$ requires $\kappa_S \ge 800$ pN·nm·rad^{-1} (*arrow*). However, to keep $\varepsilon_r = |1 - \omega_r| \le 10\%$ requires $\kappa_S \le 20$ pN·nm·rad^{-1} (*shaded region*). Other parameter values are given in the main text.

$$\xi_L \frac{d\theta_L}{dt} = F(\theta - \theta_L) + \sqrt{2k_B T \xi_L}\beta(t), \quad (2)$$

where ξ_R and ξ_L are the drag coefficients for the rotor and the load, respectively, and N is the total number of stators in the motor. V is the interaction potential between the rotor and a stator. V depends on the relative angular coordinates, $\Delta\theta_i = \theta - \theta_i^S$, where θ_i^S, the composite coordinate of stator i, consists of two parts: $\theta_i^S = \theta_i + \theta_i^c$. θ_i is the (physical) angular distance of the stator from its stationary anchoring point on the cell wall, and θ_i^c is the internal (chemical) coordinate of the stator. The load is coupled to the rotor via a nonlinear spring described by a function F, which can be determined from the hook spring compliance measurement (36). The last terms in Eqs. 1 and 2 are stochastic forces acting on the rotor and on the load, with k_B the Boltzmann constant and T the absolute temperature. $\alpha(t)$and $\beta(t)$ represent two independent white noise fluctuations of unity intensity.

The dynamics of stator position θ_i is governed by a Langevin equation:

$$\xi_S \frac{d\theta_i}{dt} = -\frac{\partial}{\partial\theta_i^S} V\left(\theta - \theta_i^S\right) - \kappa_S \theta_i + \sqrt{2k_B T \xi_S}\gamma_i(t), \quad (3)$$

where ξ_S is the drag coefficient of the stator, κ_S is the torsional spring constant of the stator spring, and $\gamma_i(t)$ is an independent white-noise fluctuation of unity intensity. Each stator stepping event changes θ_i^c by δ_0. The probability of the forward step during a time interval Δt is $P_f(\theta_i^c \to \theta_i^c + \delta_0)$. The stepping rate, P_f, is controlled by the external driving force (PMF), but it also depends on the mechanical state of the stator characterized by the torque between the rotor and the stator, $\tau_i \equiv -V'(\Delta\theta_i)$, which depends on the relative angle $\Delta\theta_i$:

$$P_f\left(\theta_i^c \to \theta_i^c + \delta_0\right) = R_f(\tau_i)\Delta t = k_f(\Delta\theta_i)\Delta t. \quad (4)$$

The key assumption in our model is that $R_f(\tau_i)$ decreases with τ_i, i.e., the forward stepping rate is higher when the stator generates torque opposite to the rotor rotation (31).

In this article, we introduce the backward stepping probability, $P_b(\theta_i^c \to \theta_i^c - \delta_0)$, which also depends on the relative angle $\Delta\theta_i$:

$$P_b\left(\theta_i^c \to \theta_i^c - \delta_0\right) = R_b(\tau_i)\Delta t = k_b(\Delta\theta_i)\Delta t. \quad (5)$$

Backward stepping happens when the stator has overreached on the FliG ring with a large value of $\Delta\theta_i$ (compared with δ_0), P_b remains near zero at $|\Delta\theta|_i \le \delta_0$ and increases as $\Delta\theta_i$ increases beyond δ_0.

We have considered different forms of stator-rotor interaction potential, starting with the linear V-shaped function, $V(\Delta\theta) = \tau_0|\Delta\theta|$, where the torque from a single stator is τ_0, with its sign depending on whether the stator is pulling ($\Delta\theta<0$) or dragging ($\Delta\theta>0$). Other forms of V, such as semiparabolic and pure parabolic potentials, are also studied. The simplest forward stepping rate depends on the sign of the force: $k_f(\Delta\theta < -\delta_c) = 0$, $k_f(-\delta_c < \Delta\theta < 0) = k_+$, $k_f(\Delta\theta > 0) = k_-(> k_+)$, with a cutoff angle δ_c introduced to prevent run-away stators (31). More complex forms of k_f and k_b are studied in the following sections. Quantitatively, we use $\tau_0 = 505$ pN·nm, $\xi_R = 0.02$ pN·nm·s·rad^{-2}, $\xi_S = k_B T/D_S = 0.008$ pN·nm·s·rad^{-2}, where $D_S = 500$ rad^2 s^{-1}, $k_+ = 12{,}000\text{s}^{-1}$, $k_- = 2k_+$, and $\delta_c = \delta_0$ unless otherwise stated. The load ξ_L varies from 0.02 to 50 pN·nm·s·rad^{-1}. The values of the stator and rotor drag coefficients, ξ_R and ξ_S, are estimated from Berg (2). A list of estimation methods and/or references for the parameter values can be found in the supplement to our previous work (31).

Maximum speed is independent of stator number and effects of stator compliance

In our previous work (31), it was shown that the maximum rotation speed (at near-zero load) is independent of the number of stators under the general condition that the stators are more likely to step forward when they generate backward torque, i.e., $r(= k_+/k_-) \le 1$. We call this scenario the force-dependent-stepping (FDS) mechanism. The (physical) locations of the stators were fixed in our previous model for simplicity. A more realistic description should take into account the finite stator compliance as the stator is tethered to the rigid peptidoglycan cell wall through an α-helix of 7–8 nm in length (30,32). Indeed, it was proposed that the independence of the zero-load speed on the stator number can be obtained by introducing a weak stator spring with an elastic constant value of $\kappa_S \approx 200$ pN·nm·rad^{-1} or smaller (27). In Fig. 1 *B*, the motor dynamics under a large load is shown with this small κ_S value (see Fig. S1 in the Supporting Material for a low-load case). The angular displacement of the stator from its anchoring point can be as large as 10δ and the angular position fluctuation reaches 2δ. The large stator position displacement and its fluctuation put in doubt this weak-stator-spring (WSS) scenario.

Here, we systematically investigate the motor dynamics for a wide range of stator spring constants. We show that adding the stator spring does not interfere with the FDS mechanism ($r \le 1$). However, very stringent constraints for the stator spring value are required in the absence of the FDS mechanism, i.e., when $r < 1$. Such stringent constraints on the stator spring constant result from two opposing requirements. The first requirement is that the stator displacement and its fluctuation should be smaller than a few δ, which sets a lower limit for the spring constant, κ_S^{min}. The second requirement is the independence of the zero-load speed on the stator number, which requires that the stator spring be soft and therefore sets a maximum value for the spring constant, κ_S^{max}.

To characterize the dependence of the zero-load speed on the number of stators, we define the zero-load speed

ratio $\omega_r \equiv \omega_0(8)/\omega_0(1)$, and the zero-load speed variation $\varepsilon_r \equiv |1-\omega_r|$, where $\omega_0(1)$ and $\omega_0(8)$ are the speed at near-zero load for stator numbers $N=1$ and $N=8$, respectively. From the recent resurrection experiments at low load (30), a conservative estimate for ε_r is ~10%. In our model with the FDS mechanism ($r<1$), the zero-load speed variation, ε_r, is <20% for all values of κ_S considered (Fig. 1 *C*), and becomes <10% for $r \le 0.5$.

For $r>1$, as in the case studied in Bai et al. (27), ϵ_r only becomes small for extremely small κ_S. Consider the case where $r=2$: κ_S has to be <20 pN·nm·rad^{-1} to have $\epsilon_r \le 10\%$. Such a weak stator spring leads to large stator position displacement and fluctuations (Fig. 1 *D*). To keep the stator displacement at $|\Delta\theta^S| \le 2\delta$, κ_S needs to be >800 pN·nm·rad^{-1}, inconsistent with the WSS scenario. This behavior is insensitive to the choices of other parameters, such as D_S (see Fig. S1, *A* and *B*, for details).

The phase diagram of our model is summarized in Fig. 2. The FDS condition $r<1$ guarantees the independence of the zero-load speed on the stator number (within the experimental error) for a wide range of stator spring constants. The standard deviation, $\sigma(\theta^S-\theta^c)$, of the stator's angular position can be calculated from our model. By requiring that $\sigma(\theta^S-\theta^c)<\theta_d/2$, with $\theta_d = 2\pi/N$ the average angular spacing between neighboring stators, we obtain a lower bound for κ_S of ~ 488 pN·nm·rad^{-1} for $N=8$. This value is similar to the theoretical estimation of the minimum spring constant for the α-helix (see Supporting Material for details). Conversely, in the absence of the FDS condition ($r>1$), there is only a small region of the parameters (r and κ_S) that can lead to both small ε_r and reasonable values of stator displacement and fluctuation. As r increases, the region of acceptable κ_S values shrinks and disappears for $r \ge 1.5$ (see Fig. 2).

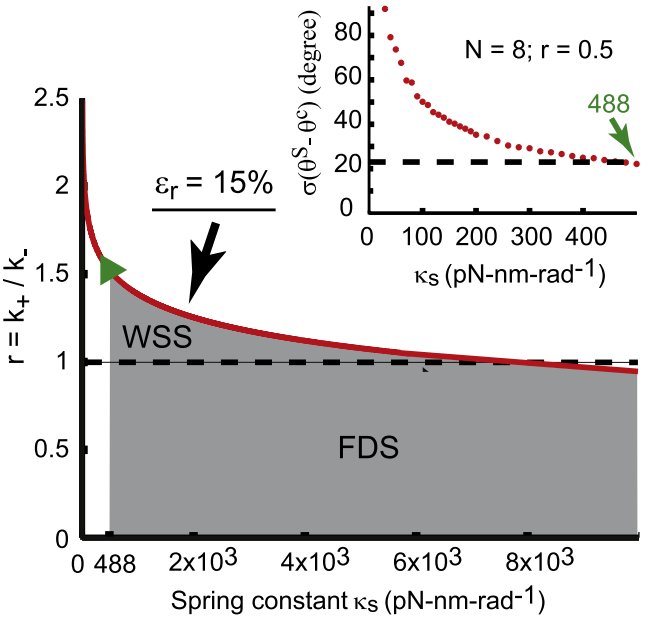

FIGURE 2 (Color online) Phase diagram of the motor behavior in parameter space (κ_S,r). The solid line (*red* color online) shows the parameter choices to achieve 15% zero-load speed variation ($\varepsilon_r = 15\%$): the parameter space below the line corresponds to $\varepsilon_r<15\%$. (*Inset*) Standard deviation $\sigma(\theta^S-\theta^c)$ (*dots*) of the angular position for individual stators for different spring constants with $N=8$, $r=0.5$, and $\xi_L = 0.002$ pN·nm·s·rad^{-2} (low load). Requiring that $\sigma(\theta^S-\theta^c) \le \theta_d/2$, with $\theta_d = 2\pi/N$, the average spacing between neighboring stators, which is ~22.5° for $N=8$, results in a minimum spring constant of ~488 pN·nm·rad^{-1}, as represented in the inset (*arrowhead*) and the main plot (*triangle*). The two requirements, i.e., small ε_r and $\sigma(\theta^S-\theta^c) \le \theta_d/2$, constrain the choices of parameters. For $r \ge 1$, κ_S needs to be small (the WSS mechanism), and the choice for κ_S is highly limited, as shown by the small gray area between the solid and dashed lines, which diminishes for $r \ge 1.5$. In contrast, for $r<1$ (the FDS mechanism), there is a large region (*gray area*) below the dashed line of allowed κ_S values with essentially no upper limit.

Rotation under external force and the stator's backward steps

An important characteristic of the BFM torque-speed curve is the absence of a barrier to backward rotation. Experiments by applying external torques to drive the motor backward (at negative speed) or forward at speeds greater than the zero-load speed can be used to discriminate between different models. For example, the thermal ratchet model proposed by Meister (23) predicted that the torque would rise sharply if the motor is driven backward. This behavior was first observed (37) but later found to be an artifact of the experimental procedure (38). Washizu et al. (39) found that motor torque is constant up to ~100 Hz for rotation in either direction, which was later confirmed by more precise study using optical tweezers (15) and more careful electrorotation experiments (33).

In our previous study (31), we did not consider backward stator steps, which are relatively rare under normal operating conditions (10). However, we expect the back jumps to become dominant when the stator is driven backward into regimes with $\Delta\theta < -\delta_c$, where the forward steps are prohibited. Here, we study the motor behavior under external driving force by including the backward steps. Intuitively, since the landing points of these backward steps are still on the positive side of the potential with positive torque τ_0, inclusion of backward steps in our model can naturally explain the observed torque continuity near stall when the motor is driven backward.

To model the external driving force, the equation of motion for the load is now modified by an additional term representing the external torque,

$$\xi_L \frac{d\theta_L}{dt} = F(\theta-\theta_L) - \tau_{ext}(t) + \sqrt{2k_BT\xi_L}\beta(t), \qquad (6)$$

where τ_{ext} is the external torque, applied in either the backward (Fig. 3 *A*) or the forward (Fig. 3 *C*) directions. The drag coefficient ξ_L for a tethered cell is roughly 5 pN·nm·*s*·rad^{-2}, in accordance with a BFM speed of ~10 Hz (40) for a tethered cell with $\tau_{ext}=0$. At a given value

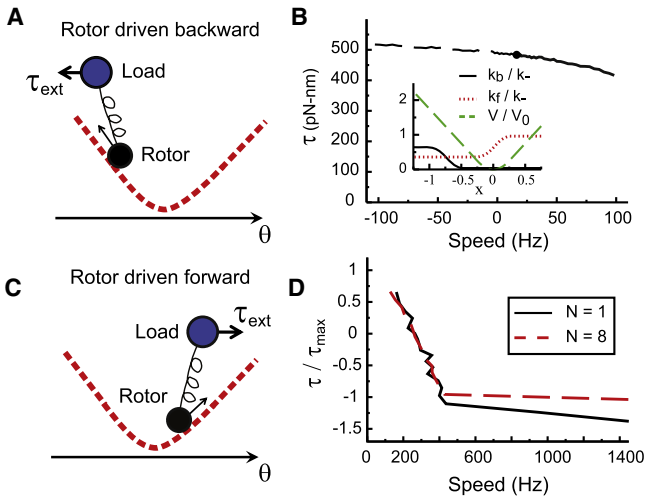

FIGURE 3 (Color online) Dynamics of the motor driven by external forces. (*A*) The backward forcing scheme. The rotor (*small black circle*) moving on the rotor-stator potential (*dashed curve*) is elastically linked to the load (*large circle*), to which an external torque is applied in the direction opposite to the force applied by the stator, given by the slope of the potential. (*B*) Torque-speed curve for $N = 1$ near stall. Starting from the black circle, the dashed black and solid lines represent the cases where the applied external torque has the opposite and the same signs, respectively, as the stator-generated torque. (*Inset*) The potential between rotor and stator (*dashed line*), and the forward and backward rates (*dotted* and *solid line*, respectively). Here, we used a semiparabolic potential: $V(x)/V_0 = 4x^2$, for $|x|<1/4$; $V(x)/V_0 = 2|x| - 1/4$, for $|x| \geq 1/4$, with $x \equiv \Delta\theta/\delta$ as the normalized angle variable and $V_0 = 15k_BT$. Other parameters used are $k_0 = 16,000s^{-1}$, $k_+ = 0.5k_0$, with $k_0 = k_- - k_+$, and $\delta_l = 0.1\delta$. (*C*) The forward forcing scheme. The applied torque is in the same direction as the rotation of the rotor. (*D*) The normalized motor torque versus speed as the motor is driven forward by external forces for $N = 1$ (*solid line*) and $N = 8$ (*dashed line*).

of τ_{ext}, the motor torque can be determined by the torque balance equation: $\xi_L\omega = \tau_{ext} + \tau$.

The forward and backward stator stepping probabilities, k_f and k_b, have opposite dependence on the relative stator-rotor angle $\Delta\theta$ (see Fig. 3 *B*, *inset*). The backward-stepping probability, k_b, is negligible near $\Delta\theta = 0$ and becomes significant when the stator is driven far away from this equilibrium position. Here, the specific forms of k_f and k_b for stator i are chosen to be

$$k_f(\Delta\theta_i) = k_+ + k_0[1 + \exp(\tau_i\delta\theta_l/k_BT)]^{-1}, \quad (7)$$

$$k_b(\Delta\theta_i) = k_0[1 + \exp(-\tau_{bi}\delta\theta_l/k_BT)]^{-1}, \quad (8)$$

where $\tau_i = -V'(\Delta\theta_i)$, $\tau_{bi} = -V'(\Delta\theta_i + 0.75\delta)$. Equation 7 for k_f can be understood as the continuous version of the discrete forward-stepping rate used in our previous study (31), where $k_0 = k_- - k_+$ and $\delta\theta_l$ determines the size of the transition region between k_+ and k_-. A semiparabolic potential is used here (Fig. 3 *B*); the results do not change when a V-shaped potential and other expressions for the stepping rates are used, as long as the stepping rates follow the same general trends as shown in the inset of Fig. 3 *B*.

Fig. 3 *B* shows the torque-speed curve with $N = 1$ when an external torque is applied to make the rotor rotate backward. In agreement with the experiments, the motor torque varies only slightly with speeds up to 100 Hz in both directions without any barrier (see Supporting Material for the case $N = 8$). The other regime outside of the normal motor operating range is when the external torque is applied along the same direction as the motor's natural rotation. As measured by Turner et al. (34), when the motor speed is driven beyond its intrinsic maximum speed, the torque generated by the motor drops below zero linearly with the speed before it levels off at a maximum negative torque. Fig. 3 *D* shows that our model reproduces this behavior. The reason why the torque levels off at $\sim -\tau_0$ can be understood from our model, as shown in Fig. 3 *C*. As the external torque forces the motor to move faster than its natural maximum speed at low load, the stators spend most of their time in the negative torque regime of the rotor-stator potential, where the maximum value of the torque is equal to $-\tau_0$, for the symmetric potential used in our model. To the extent that the observed maximum negative torque at super high speed is comparable to the motor's natural maximum positive torque, the data in Turner et al. (34) show that the rotor-stator potential is approximately symmetric.

Taken together, our model with one unified set of parameters can generate the whole torque-speed curve, from the negative-speed regime, to the normal operating regime with positive torque and speed, and to the negative-torque regime. Fig. S8 shows the full torque-speed curve in all three regimes. Our model is validated by its agreement with available experiments in the three regions of the (τ-ω) plane.

Temperature and isotope effects and thermally activated stepping

Changing temperature affects all the transition rates, in particular the stepping rates. The temperature dependence of k_+ and k_- in our model leads to changes in the so-called knee speed, ω_n, and the speed near zero load, ω_0, without changing the maximum torque at stall, consistent with experimental observations (37,41). Here, we investigated quantitatively the temperature effects on the torque-speed curve, motivated by a recent experiment (35) that extended previous studies (32) of thermal effects on motor rotation at the high-load regime to the near-zero load regime within a temperature range from 9 to 37°C. It was found that the maximum speed changes nearly exponentially with temperature, and with an activation enthalpy of $\Delta G_a = 52$ kJ/mol.

For simplicity, we consider a V-shaped stator-rotor interaction potential, with the temperature dependence of the stepping rates following the simple Arrhenius law:

$$k_\pm = k_{\pm 0}\exp(-\Delta E_a/k_BT), \quad (9)$$

where ΔE_a is the free-energy barrier for a stator to step. The torque dependence of the stepping rate is included by having a different prefactor, k_{-0} or k_{+0}, when the stator is generating negative or positive torque, respectively ($k_{-0}/k_{+0} = 2$ used here). From ΔG_a, we obtain $\Delta E_a = 52$ kJ/(6.02 $\times$ 10^{23}) = 8.6 $\times$ 10^{-20} J $\approx$ 0.54 eV. The temperature dependence of speed near zero load can be determined from our model by using Eq. 9. The model results (Fig. 4 *A*) are in excellent agreement with the experiment data for all temperatures measured with only one fitting parameter, $k_{-0} = 1.6 \times 10^{13}$ s^{-1}.

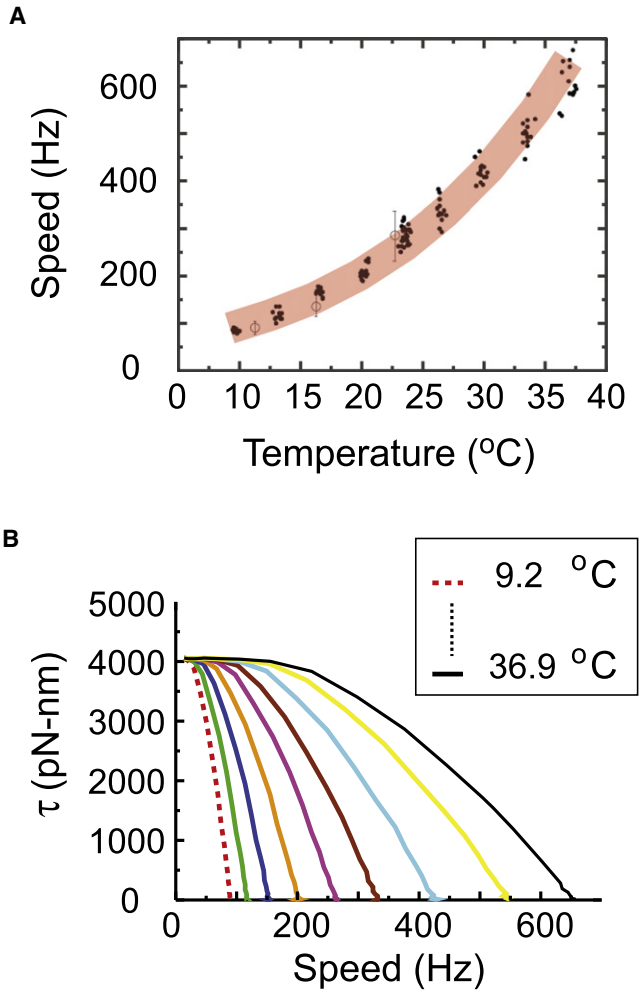

FIGURE 4 (Color online) The temperature dependence of the torque-speed curves. (*A*) Speed near zero load as a function of temperature. The thick curve is from numerical simulations of our model. The width of the curve corresponds roughly to the fluctuation of the maximum speed. Black dots are data points from experiments by Yuan and Berg (35). The three open circles with error bars are data from other studies by Berg and colleagues (11,37). (*B*) Torque-speed curves at different temperatures with $N = 8$. Starting at the dotted line at the left, temperature values are: 9.2, 12.6, 16.1, 19.8, 23.5, 26.8, 30.4, 34.2, and 36.9°C. A V-shaped potential is used and the parameters for the stepping rates in Eq. 9 are: $\Delta E_a = 8.6 \times 10^{-20}$ J, $k_{0-} = 2k_{0+} = 1.6 \times 10^{13}$ s^{-1}.

As shown in Fig. 4 *B*, at high loads, the motor torque is independent of temperature. As explained in our previous work (31), this is due to the fact that at high loads, each stator spends most of its time generating positive torque, τ_0, independent of the stepping events, and therefore, the maximum torque $\tau_{max} \approx N\tau_0$ is independent of temperature.

A possible mechanism for the torque-dependent stepping rate is that there is a torque-dependent contribution to the energy barrier for stepping. In the linear approximation, this torque-dependent term can be expressed as $\Delta\Delta E_a(\tau) \approx \tau\delta_l$, where δ_l can be interpreted as the size of the (angular) conformational change of the stator's transition state relative to its prestepping state. For the simple V-shaped potential considered here, we have $k_{\pm 0} \approx k_a \exp(\mp\tau_0\delta_l/k_BT)$, where k_a is the intrinsic molecular fluctuation frequency or the reaction attempting rate. A lower bound for δ_l can be estimated from the characteristic torque, τ_0, and the value of $r = k_+/k_-$: $\delta_l \geq k_BT/2\tau_0 \ln(1/r)$, which is ~0.2 – 0.5° for $r = 0.5$ and $\tau_0 = 175 - 500$ pN·nm. Note that this torque-dependent contribution, $\Delta\Delta E_a(\tau)$, to the energy barrier is much smaller than ΔE_a. Therefore, for the relatively small temperature range ($\Delta T/T \sim 10\%$) considered here, the torque-dependent prefactors k_{-0} and k_{+0} can be approximated as temperature-independent.

According to the transition-state theory (42) with harmonic approximation, the attempt rate, k_a, for stepping should be proportional to $\sqrt{f/m}$, where f is the stiffness of the harmonic-energy landscape of the system and m is the mass of the reacting element. For flagellar motors driven by the PMF, the stepping rates should be proportional to $1/\sqrt{m}$, where m is the mass of the particle flowing through the channel. Hence, assuming that f is independent of the solvent, the intrinsic maximum speed of the flagellar motor near zero load should be scaled by $\sqrt{2}$ when changing the operating environment from water (H_2O) to heavy water (D_2O), i.e., when the proton-carrying particle changes from the hydrogen ion, H^+, to the deuterium ion, D^+. This isotope effect has indeed been observed (35).

General properties of the torque (force)-speed relationship and the CW-CCW asymmetry in BFMs

The most important and measurable biophysical property of a molecular motor is its force-speed curve (for linear motor) or torque-speed curve (for rotatory motor). Here, we study how the overall shape of the torque-speed ($\tau - \omega$) curve depends on the stator-rotor interaction potential and the stator stepping rate.

For the V-shaped potential, the $\tau - \omega$ curve is concave. We now consider a parabolic potential (Fig. 5, *A* and *B*, *insets*) with the stepping rates

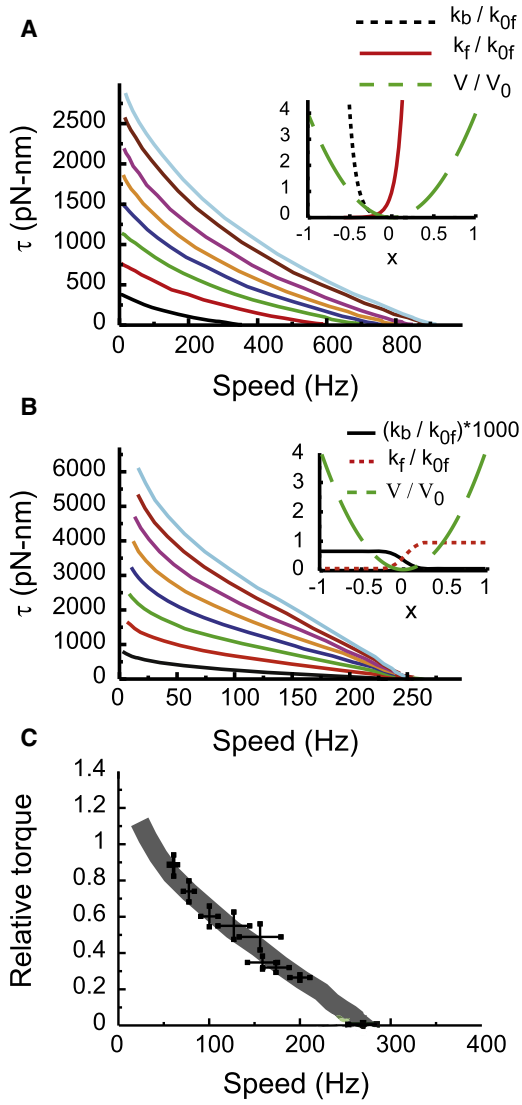

FIGURE 5 (Color online) The torque-speed relationship with a parabolic interaction potential. The parabolic potential is $V(x) = 4V_0x^2$, with $x \equiv \Delta\theta/\delta$ as the normalized angle variable and $V_0 = 15k_BT$. Different numbers of stators, $N = 1$–8, and different stepping rates are used. (*A*) Torque-speed curves with unbounded stepping rates as given by Eqs. 10 and 11 with parameter values $k_{0f} = 12,000\ s^{-1}$ and $k_{0b} = 120\ s^{-1}$. (*Inset*) The dashed-dotted line represents the backward stepping rate, the solid line the forward stepping rate, and the dashed line the parabolic stator-rotor potential. (*B*) Torque-speed curves with bounded stepping rates are given by Eqs. 12 and 13, with parameter values $k_{0f} = 30,000\ s^{-1}$, $k_{0b} = 30s^{-1}$, and $E_0 = 0.1\tau_0\delta\theta_l$. (*Inset*) Stepping rates and potential, as in *A*. Parameter values common to *A* and *B* are $\kappa_S = 10^5$ pN·nm·rad^{-1}, $D_S = 500$rad^2 s^{-1}, and $\delta\theta_l = 0.1\delta$. (*C*) Normalized torque-speed curve for CW rotation. Black symbols with error bars are experimental data from Yuan et al. (19). Gray transparent line represents the model results, with $k_{0f} = 32,000\ s^{-1}$ and $N = 8$. All other parameters have the same value as in *B*. Simulation results (*gray curve*) are normalized by the first experimental data at ~61 Hz.

$$k_f(\Delta\theta_i) = k_{0f}\exp(-\tau_i\delta\theta_l/k_BT) \quad (10)$$

and

$$k_b(\Delta\theta_i) = k_{0b}\exp(\tau_i\delta\theta_l/k_BT), \quad (11)$$

which depends exponentially on the torque, $\tau_i(= -V'(\Delta\theta_i))$, for the forward and backward steps with constants k_{0b}, k_{0f}, and $\delta\theta_l$. Fig. 5 *A* shows the torque-speed curves for different values of N. The torque-speed curves are slightly convex, almost linear. Another interesting finding is that for the stepping rates given in Eqs. 10 and 11, the maximum speed at low load increases with N. This dependence of ω_0 on N is a consequence of the unbounded exponential increase of the forward stepping rate in the negative torque regime. As the number N of stators increases, the positions of the stators in the waiting phase can be pushed into regimes with larger values of negative torque due to the quadratic nature of the potential. The resulting larger forward stepping rates, according to Eq. 10, lead to higher maximum speeds for larger N.

To maintain the independence of ω_0 on N, the stepping rates need to saturate to a maximum value as $|\tau_i|$ increases:

$$k_f(\Delta\theta_i) = k_{0f}[1 + \exp((\tau_i\delta\theta_l + E_0)/k_BT)]^{-1}, \quad (12)$$

$$k_b(\Delta\theta_i) = k_{0b}[1 + \exp(-(\tau_i\delta\theta_l + E_0)/k_BT)]^{-1}. \quad (13)$$

Here, E_0 and $\delta\theta_l$ set a critical torque, $\tau_c = E_0/\delta\theta_l$, beyond which the forward stepping rate saturates. The independence of maximum speed on stator number is recovered for $\tau_c \approx 0.1\tau_0$ (Fig. 5 *B*). This behavior is independent of the specific values of τ_c and $\delta\theta_l$ (see Fig. S5, *A* and *B*, for cases of $\tau_c = 0.2\tau_0$ and different values of $\delta\theta_l$).

Until very recently, it was assumed that CCW and CW rotation are symmetric and exhibit the same torque-speed relationship (43). However, Yuan et al. (19) recently measured the torque-speed relationship for an *E. coli* strain locked in CW rotation and found a quasilinear torque-speed curve, different from that of the CCW rotating BFM. Here, by using the parabolic potential and bounded stepping rates (Eqs. 12 and 13), our model generates a torque-speed curve that is in quantitative agreement with the measured CW torque-speed curve (19) (Fig. 5 *C*).

Aside from the stator-rotor interaction, the stepping-rate ratio, r, also affects the characteristics of the torque-speed dependence. Fig. 6 *A* shows the torque-speed curves for two different values of r, $r = 2$ and $r = 0.5$. For $r = 0.5$, the torque, τ, decreases as the speed, ω, increases. However, for $r = 2$, the slope of the torque-speed curve changes its sign after the knee region from negative to positive, giving rise to a nonmonotonic dependence of speed on torque (or load). The same behavior is observed when stator springs are included (see Fig. S4, *A* and *B*).

The mechanism for this behavior can be understood by studying two timescales, the average moving time $\langle t_m \rangle$ and the average waiting time $\langle t_w \rangle$ (31). The dependence of these timescales on motor speed are shown in Fig. 6 *B* for

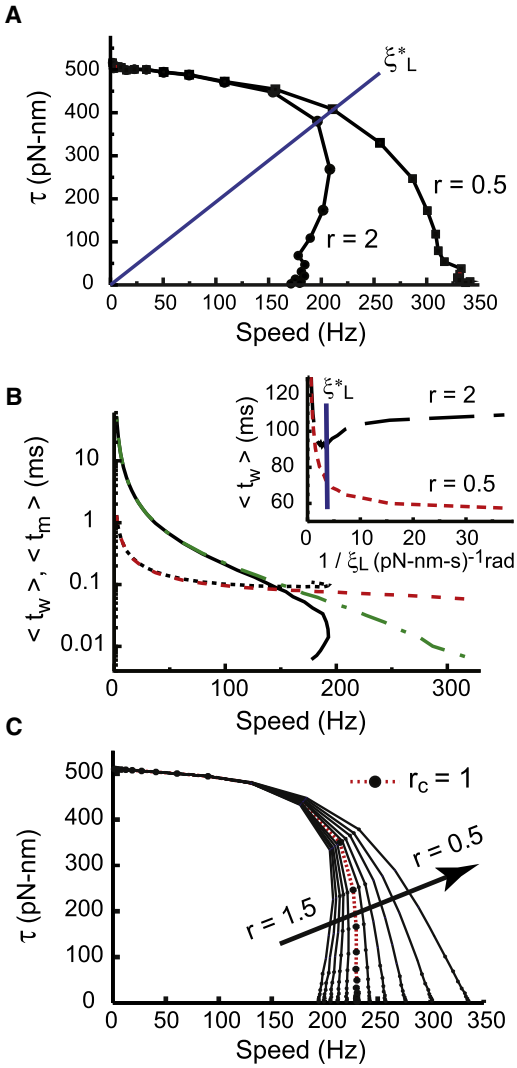

FIGURE 6 (Color online) The dependence of the torque-speed curve on the stepping rate ratio r. (*A*) The torque-speed ($\tau-\omega$) curves for $r = 0.05$ (*solid line with squares*) and $r = 2$ (*solid line with circles*), both with $N = 1$. (*B*) The average waiting time, t_w, for $r = 0.05$ (*dotted line*) and $r = 2$ (*dash-dotted line*), and the average moving time, t_m, for $r = 0.05$ (*dashed line*) and $r = 2$ (*solid line*) as functions of the rotational speed. (*Inset*) Zoom of the average waiting time, t_w, as a function of the inverse of the load, ξ_L, for the two cases $r = 2$ (*dashed line*) and $r = 0.05$, (*dotted line*). (*C*) The torque-speed ($\tau-\omega$) curves for 11 different values of r, from 1.5 to 0.5. The dotted line represents the curve corresponding to the critical value $r_c = 1$.

both $r = 0.5$ and $r = 2$. Note the different dependence of $\langle t_w\rangle$ on the load, ξ_L, for $r = 0.5$ and $r = 2$ (Fig. 6 *B*, *inset*). At a specific value of the load, ξ_L^*, close to the knee, where the torque-speed curves of the two cases ($r = 0.5$and $r = 2$) start to diverge, the dependence of the average waiting time, $\langle t_w\rangle$, on ξ_L also becomes qualitatively different. Whereas $\langle t_w\rangle(r = 0.5)$ continues to decrease and eventually level off at ~60 μs near zero load, $\langle t_w\rangle(r = 2)$starts to increase at ξ_L^* to a higher value, ~110 μs, almost twice the value for $r = 0.5$. This is caused by the fact that for $r>1$, it is harder to step when the stator spends more time in the negative torque regime at lower load, because $k_-<k_+$. This increase in waiting time for $\xi_L<\xi_L^*$ leads to a decrease in motor speed as the load is lowered (below ξ_L^*) for $r = 2$ (Fig. 6 *A*). In Fig. 6 *C*, the $\tau-\omega$ curves are shown for $r = 0.5-1.5$. It is clear that the torque-speed derivative $(\partial\tau/\partial\omega)$ at the knee goes from positive to negative when r goes from 1.5 to 0.5, with a critical value $r_c = 1$.

In the model studied by Xing and colleagues (26,27), the stepping rate has a complicated dependence on the relative angle between the stator and the rotor and in general favors stepping in the positive torque regime, which corresponds to $r>1$ in our model. Indeed, the torque-speed curve from (26,27) shows a change of sign in the torque-speed derivative at around the knee (see Fig. 2 *B* in Bai et al. (27)). Such a nonmonotonic torque-speed dependence is not observed in experiments, which lends further support to having $r\leq 1$ (or the equivalent), i.e., the FDS mechanism.

DISCUSSION

In this article, our original model for the BFM (31) is extended to incorporate several key biological ingredients, such as stator back-steps, stator compliance, temperature dependence of the stepping rate, and rotational (CW-CCW) asymmetry. Our model connects the microscopic details of the flagellar motor, such as the stator-rotor interaction potential and the stator stepping rate, with the macroscopic measurements, in particular, the torque-speed dependence. A summary and discussion of the specific findings are given below.

Backward rotation

The introduction of a torque-dependent back-stepping rate reproduces the observed continuity of the torque-speed curve near stall (high load). We proposed that the back-stepping is dominant in the far-positive side of the V-shaped potential, where it prevents the system from going into the unphysical regime with very large stator-rotor displacement. Since the landing points of these back-steps are still on the positive side of the potential, with the same positive torque τ_0, inclusion of back-steps in our model naturally explains the observed continuous torque-speed relation across the stalling point, when the motor is driven backward. For models with periodic potentials (26,27,29), backward rotation could lead the system (temporally) into the negative torque regime before reentering the positive torque regime. This would not necessarily affect the average torque-speed behavior, such as the absence of barrier to backward rotation, but would lead to large fluctuations in rotational speed or the required external torque, which may be tested by future experiments. See the Supporting Material for a detailed discussion of periodic potentials.

Effects of stator springs

Thorough analysis of parameter dependence of speed at near-zero load shows that adding the stator spring preserves our original model results for all ranges of spring constant values, as long as $r \leq 1$. For $r>1$, however, the stator spring constant needs to be exceedingly weak, and such a weak stator spring gives rise to unrealistically large displacements and fluctuations of stator positions.

Characteristics of the torque-speed relationship

Our study shows that the torque-speed curve is generally determined by two factors: the power-stroke potential and the dependence of stepping rates on the mechanical coordinate. We demonstrate here that changing the ratio of stepping rates, $r = k_+/k_-$, can change the torque-speed dependence from monotonic to nonmonotonic, and changing the potential from linear to quadratic can lead the torque-speed curve to change from concave to convex.

The recently measured torque-speed curve for the CW rotating BFM (19) can be reproduced quantitatively by our model with a parabolic stator-rotor interaction potential. Such a quasilinear torque-speed curve can also be obtained with a V-shaped potential by setting the stepping rate k_+ close to zero, as shown in our previous work (31). In the low to medium load regime studied in recent experiments, these two possible mechanisms generate the same quasilinear torque-speed relationship. However, at high load, the parabolic potential leads to a superlinear increase of the torque, whereas the small k_+ scenario leads to a constant torque near stall. A measurement of the torque-speed relation near stall for the CW rotation is needed to distinguish these two scenarios. The experimental data are fitted better by having a bounded stepping rate, which (as shown in Fig. 5 *B*) leads to the independence of the speed near zero load on the number of stators for both the CW- and CCW-rotating motors. This prediction can be checked with resurrection experiments for CW motor at low load.

We note that the convex torque-speed curve for the parabolic operating potential is similar to the force-velocity curves of the linear motor kinesin-1 at high load (18,16). The independence of the maximum velocity on the number of power generators also agrees with current theoretical models for linear kinesin-1 motor (44) and for linear myosin motor systems (45). These similarities suggest that our simple modeling framework may be used to understand the general force-speed dependence of different molecular motors.

Chemical and mechanical gating of the stepping process

From the measured temperature dependence of the maximum speed, our model shows that the stator stepping process is thermally activated with a free energy barrier $\Delta E_a \sim 0.5$ eV, which is comparable to the energy available from a proton moving down the transmembrane PMF (~0.17 eV for $\Delta p = -170$ mV). Current models, which consider detailed gating mechanisms for proton translocation, have reported different behaviors. Xing and colleagues (26,27) predicted that the speed at low load would increase almost linearly with membrane voltage. Mora et al. (28) predicted that both torque and speed would grow sublinearly with PMF. Neither predictions can be ruled out by experiments that indirectly show a linear PMF dependence in a relatively small range of rotation speed between 80 and 270 Hz (46). Direct measurements of PMF dependence at near-zero load are needed to elucidate the exact electrochemical gating mechanism of the stator stepping process.

Besides PMF, there may be a mechanical contribution to the energy barrier for stepping $\Delta\Delta E_a(\tau)$, which accounts for the torque(τ)-dependent stepping rate. This mechanical gating energy may be small (~0.35 k_BT for $r = 0.5$), but its effects are significant, as shown here and previously (31). A lower bound for the conformational change (~0.2–0.5° in angle or ~0.8–2 Å in distance) in the transitional state of the stator can be deduced from the mechanical gating energy and the maximum torque generated by a single stator.

SUPPORTING MATERIAL

Additional text, references, and nine figures are available at http://www.biophysj.org/biophysj/supplemental/S0006-3495(11)00296-7.

We thank Drs. Junhua Yuan and Howard Berg for many stimulating discussions.

This work was partially supported by a National Institutes of Health grant to Y.T. (R01 GM-081747).

REFERENCES

1. Berg, H. C., and R. A. Anderson. 1973. Bacteria swim by rotating their flagellar filaments. *Nature.* 245:380–382.
2. Berg, H. C. 2003. The rotary motor of bacterial flagella. *Annu. Rev. Biochem.* 72:19–54.
3. Sowa, Y., and R. M. Berry. 2008. Bacterial flagellar motor. *Q. Rev. Biophys.* 41:103–132.
4. Thomas, D. R., N. R. Francis, …, D. J. DeRosier. 2006. The three-dimensional structure of the flagellar rotor from a clockwise-locked mutant of *Salmonella enterica* serovar Typhimurium. *J. Bacteriol.* 188:7039–7048.
5. Kojima, S., and D. F. Blair. 2001. Conformational change in the stator of the bacterial flagellar motor. *Biochemistry.* 40:13041–13050.
6. Ryu, W. S., R. M. Berry, and H. C. Berg. 2000. Torque-generating units of the flagellar motor of *Escherichia coli* have a high duty ratio. *Nature.* 403:444–447.
7. Brown, P. N., M. A. Mathews, …, D. F. Blair. 2005. Crystal structure of the flagellar rotor protein FliN from *Thermotoga maritima*. *J. Bacteriol.* 187:2890–2902.
8. Brown, P., C. Hill, and D. F. Blair. 2002. Crystal structure of the middle and C-terminal domains of the flagellar motor protein FliG. *EMBO J.* 21:3225–3234.

9. Lloyd, S. A., F. G. Whitby, …, C. P. Hill. 1999. Structure of the C-terminal domain of FliG, a component of the rotor in the bacterial flagellar motor. *Nature.* 400:472–475.
10. Sowa, Y., A. D. Rowe, …, R. M. Berry. 2005. Direct observation of steps in rotation of the bacterial flagellar motor. *Nature.* 437:916–919.
11. Chen, X. C., and H. C. Berg. 2000. Torque-speed relationship of the flagellar rotary motor of *Escherichia coli*. *Biophys. J.* 78:1036–1041.
12. Sowa, Y., H. Hotta, …, A. Ishijima. 2003. Torque-speed relationship of the Na^+-driven flagellar motor of *Vibrio alginolyticus*. *J. Mol. Biol.* 327:1043–1051.
13. Fahrner, K. A., W. S. Ryu, and H. C. Berg. 2003. Biomechanics: bacterial flagellar switching under load. *Nature.* 423:938.
14. Reid, S. W., M. C. Leake, …, R. M. Berry. 2006. The maximum number of torque-generating units in the flagellar motor of *Escherichia coli* is at least 11. *Proc. Natl. Acad. Sci. USA.* 103:8066–8071.
15. Berry, R. M., and H. C. Berg. 1997. Absence of a barrier to backwards rotation of the bacterial flagellar motor demonstrated with optical tweezers. *Proc. Natl. Acad. Sci. USA.* 94:14433–14437.
16. Schnitzer, M. J., K. Visscher, and S. M. Block. 2000. Force production by single kinesin motors. *Nat. Cell Biol.* 2:718–723.
17. Lan, G., and S. X. Sun. 2005. Dynamics of myosin-V processivity. *Biophys. J.* 88:999–1008.
18. Visscher, K., M. J. Schnitzer, and S. M. Block. 1999. Single kinesin molecules studied with a molecular force clamp. *Nature.* 400:184–189.
19. Yuan, J., K. A. Fahrner, …, H. C. Berg. 2010. Asymmetry in the clockwise and counterclockwise rotation of the bacterial flagellar motor. *Proc. Natl. Acad. Sci. USA.* 107:12846–12849.
20. Berry, R. M. 1993. Torque and switching in the bacterial flagellar motor. An electrostatic model. *Biophys. J.* 64:961–973.
21. Braun, T. F., S. Poulson, …, D. F. Blair. 1999. Function of proline residues of MotA in torque generation by the flagellar motor of *Escherichia coli*. *J. Bacteriol.* 181:3542–3551.
22. Läuger, P. 1988. Torque and rotation rate of the bacterial flagellar motor. *Biophys. J.* 53:53–65.
23. Meister, M., S. R. Caplan, and H. C. Berg. 1989. Dynamics of a tightly coupled mechanism for flagellar rotation. Bacterial motility, chemiosmotic coupling, protonmotive force. *Biophys. J.* 55:905–914.
24. Schmitt, R. 2003. Helix rotation model of the flagellar rotary motor. *Biophys. J.* 85:843–852.
25. Walz, D., and S. R. Caplan. 2000. An electrostatic mechanism closely reproducing observed behavior in the bacterial flagellar motor. *Biophys. J.* 78:626–651.
26. Xing, J., F. Bai, …, G. Oster. 2006. Torque-speed relationship of the bacterial flagellar motor. *Proc. Natl. Acad. Sci. USA.* 103:1260–1265.
27. Bai, F., C. J. Lo, …, J. Xing. 2009. Model studies of the dynamics of bacterial flagellar motors. *Biophys. J.* 96:3154–3167.
28. Mora, T., H. Yu, and N. S. Wingreen. 2009. Modeling torque versus speed, shot noise, and rotational diffusion of the bacterial flagellar motor. *Phys. Rev. Lett.* 103:248102.
29. van Albada, S. B., S. Tănase-Nicola, and P. R. ten Wolde. 2009. The switching dynamics of the bacterial flagellar motor. *Mol. Syst. Biol.* 5:316.
30. Yuan, J., and H. C. Berg. 2008. Resurrection of the flagellar rotary motor near zero load. *Proc. Natl. Acad. Sci. USA.* 105:1182–1185.
31. Meacci, G., and Y. Tu. 2009. Dynamics of the bacterial flagellar motor with multiple stators. *Proc. Natl. Acad. Sci. USA.* 106:3746–3751.
32. Khan, S., and H. C. Berg. 1983. Isotope and thermal effects in chemiosmotic coupling to the flagellar motor of *Streptococcus*. *Cell.* 32: 913–919.
33. Berry, R. M., and H. C. Berg. 1999. Torque generated by the flagellar motor of *Escherichia coli* while driven backward. *Biophys. J.* 76: 580–587.
34. Turner, L., S. R. Caplan, and H. C. Berg. 1996. Temperature-induced switching of the bacterial flagellar motor. *Biophys. J.* 71:2227–2233.
35. Yuan, J., and H. C. Berg. 2010. Thermal and solvent-isotope effects on the flagellar rotary motor near zero load. *Biophys. J.* 98:2121–2126.
36. Block, S. M., D. F. Blair, and H. C. Berg. 1989. Compliance of bacterial flagella measured with optical tweezers. *Nature.* 338:514–518.
37. Berg, H. C., and L. Turner. 1993. Torque generated by the flagellar motor of *Escherichia coli*. *Biophys. J.* 65:2201–2216.
38. Berry, R. M., and H. C. Berg. 1996. Torque generated by the bacterial flagellar motor close to stall. *Biophys. J.* 71:3501–3510.
39. Washizu, M., Y. Kurahashi, …, H. Hotani. 1993. Dielectrophoretic measurement of bacterial motor characteristic. *IEEE Trans. Ind. Appl.* 29:286–294.
40. Silverman, M., and M. Simon. 1974. Flagellar rotation and the mechanism of bacterial motility. *Nature.* 249:73–74.
41. Chen, X. C., and H. C. Berg. 2000. Solvent-isotope and pH effects on flagellar rotation in *Escherichia coli*. *Biophys. J.* 78:2280–2284.
42. Laidler, K. J., and M. C. King. 1983. The development of transition-state theory. *J. Phys. Chem.* 15:2657–2664.
43. Blair, D. F., and H. C. Berg. 1988. Restoration of torque in defective flagellar motors. *Science.* 242:1678–1681.
44. Kunwar, A., M. Vershinin, …, S. P. Gross. 2008. Stepping, Strain Gating, and an Unexpected Force-Velocity Curve for Multiple-Motor-Based Transport. *Curr. Biol.* 18:1173–1183.
45. Lan, G., and S. X. Sun. 2005. Dynamics of myosin-driven skeletal muscle contraction: I. Steady-state force generation. *Biophys. J.* 88: 4107–4117.
46. Gabel, C. V., and H. C. Berg. 2003. The speed of the flagellar rotary motor of Escherichia coli varies linearly with protonmotive force. *Proc. Natl. Acad. Sci. USA.* 100:8748–8751.